Granular Matter (2016) 18:51
DOI 10.1007/s10035-016-0621-5

ORIGINAL PAPER

# Microstructure evolution of granular soils in cyclic mobility and post-liquefaction process

**Gang Wang**[1] · **Jiangtao Wei**[1]

Received: 12 May 2015
© Springer-Verlag Berlin Heidelberg 2016

**Abstract** Understanding the evolution of microstructure in granular soils can provide significant insights into constitutive modeling of soil liquefaction. In this study, micromechanical perspectives of the liquefaction process are investigated using the Discrete Element simulation. It is observed that during various stages of undrained cyclic loading, the soil exhibits definitive change in the load-bearing structure, indicated by evolution of the coordination number and non-affine displacements. A new particle-void fabric, termed as "centroid distance", is also proposed to quantify the evolution of particles and voids distribution in the granular packing. The fabric index is found to have strong correlation with cyclic mobility and post-liquefaction deformation of granular soils. Evolution of the fabric index indicates that particles and voids redistribute irreversibly before and after liquefaction. A highly anisotropic particle-void structure and loading-bearing capacity can be formed in the post liquefaction stage.

**Keywords** Cyclic mobility · Post-liquefaction · DEM · Microstructure evolution

## 1 Introduction

Understanding the fundamental mechanism of soil liquefaction is one of the major challenges in geotechnical earthquake engineering and soil dynamics. In general, liquefaction refers to a range of phenomena related to the increase of pore water pressure in a saturated or nearly saturated soil under cyclic loading, including flow liquefaction and cyclic mobility [13]. Flow liquefaction often occurs in a very loose soil, characterized by a sudden loss of its strength and stiffness. Subsequently, the soil will develop uncontrolled large deformation and a flow-type failure [12]. On the other hand, cyclic mobility may occur in almost all types of granular soils including dense sands. It is characterized by progressive reduction in effective stress and progressive accumulation of limited shear deformation [3].

Both flow liquefaction and cyclic mobility have caused severe damage to civil structures during the past earthquakes. Case histories learnt from significant earthquakes in recent 40 years have led to many important advances in developing empirical or semi-empirical procedures to assess potentials and the consequences of liquefaction [10,11,22,36]. Many laboratory tests have been conducted to assess the initiation of liquefaction in sandy, silty and gravelly soils, as well as the influence of various factors on the liquefaction potential, including the initial density, fine content, cyclic stress ratio (CSR), confining pressure and initial static stress etc. (e.g., [2,21,30,33]). However, most laboratory investigations can only measure the overall macroscopic behaviors of the soil. It is difficult to interpret the microscopic behaviors of the soil response from the test results. Advanced constitutive models have also been developed to describe the macroscopic stress–strain responses of liquefiable soils (e.g., [5,6,31,32,34,38]). However, all these models are phenomenological in nature, involving a variety of hypotheses and quantities that may not be physically measurable. The microstructure information of the soil has not yet been well incorporated in these models.

In recent years, Discrete Element Method (DEM) has been widely used to study the micromechanical behaviors of gran-

This article is part of the Topical Collection on Micro origins for macro behavior of granular matter.

✉ Gang Wang
gwang@ust.hk

[1] Department of Civil and Environmental Engineering, The Hong Kong University of Science and Technology, Clear Water Bay, Kowloon, Hong Kong

Published online: 23 June 2016

ular soils (e.g. [17]). In micromechanics, soil "fabric" is an all-encompassing term used to describe the arrangement of particles, particle groups and void spaces etc. in the soil [14, 15,24,25]. The microstructure of a granular assemblage can be manifested by a variety of fabric indices, such as the numbers of contacts, orientation of contact normal, orientation of branch vector, as well as orientation of particles and voids etc.

DEM simulation can be conveniently used to examine particle-by-particle response as well as evolution of the soil structure and fabric that cannot be directly observed from conventional laboratory tests (e.g. [8,9,18,19,28]). However, most of the previous studies focus on non-liquefiable soils under monotonic loading. In contrast, DEM studies on the cyclic liquefaction have been quite limited. Among a few examples, Ng and Dobry [16] verified the capability of DEM in capturing the cyclic liquefaction phenomenon in granular soils. The influence of particle shape on liquefaction initiation was evaluated by Ashmawy et al. [1]. Sitharam et al. [26] also investigated the evolution of internal variables during post-liquefaction under undrained monotonic loading.

It is worth pointing out that most previous micromechanical investigations are based on the information of particle contacts and inter-particle forces. These micro information can be homogenized to formulate a variety of fabric tensors to describe the macro properties of the assemblage. For example, the well-known "fabric tensor" by Satake [20] and Rothenburg and Bathurst [19] is constructed using normal vectors of inter-particle contact to characterize the load-bearing structure of the soil [9,37]. Fabric quantification of liquefied soils is in particular challenging because most fabric tensors are defined on contacts while liquefaction is a state that soil loses nearly all contact points. For this purpose, a new fabric index termed as the "centroid distance" $D_c$, is developed in this paper to describe the particle-void arrangement. The microstructure evolution of the granular packing in the cyclic mobility and post-liquefaction process will be studied using the new index. The micromechanical study can provide significant insight into a deeper understanding of the fundamental mechanisms of soil liquefaction.

## 2 Discrete element simulation of cyclic liquefaction

In this study, an open source DEM code, Yade [27], is used to conduct numerical simulations of granular soils under undrained cyclic simple-shear tests. First, a total of 4000 disk-shaped (2D) particles are randomly generated within a $30 \times 30$ mm representative volume element (RVE). The radius of particles ranges from 0.15 to 0.45 mm and the mean radius $R_{50}$ is 0.3 mm. Periodic boundary is prescribed on this RVE to eliminate the non-uniformity induced by the boundary. After the particles were generated, the packing was isotropically consolidated under an initial confining pressure of 100 kPa.

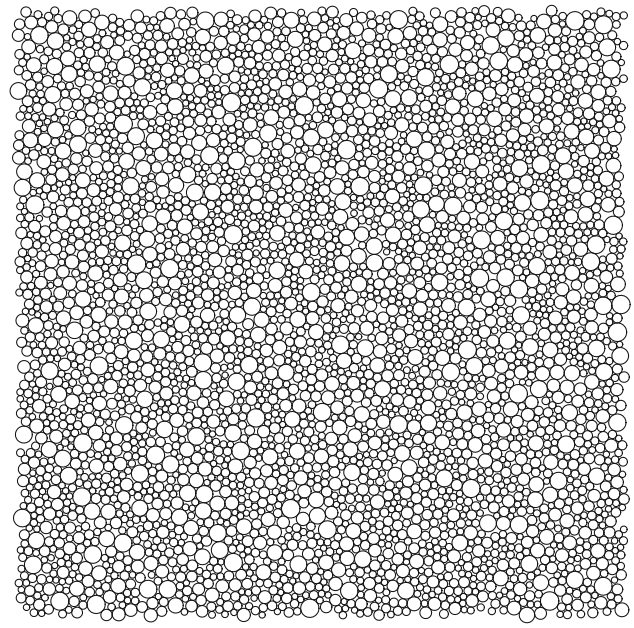

**Fig. 1** Particle configuration of a granular packing

Packings with different void ratios can be obtained by specifying different inter-particle frictional coefficients during the consolidation stage. Figure 1 shows the particle configuration with a void ratio of 0.228. Young's modulus of 70 GPa, Poisson's ratio of 0.3 and frictional coefficient of 0.5 are assigned to all the particles. These values are similar to those frequently used in previous DEM simulations of quartz sands (e.g. [26,28]). A nonlinear Hertz-Mindlin model is used to describe the particle contact behaviors in loading and unloading. Unless it is stated otherwise, all analyses presented in this paper are based on simulations using this packing.

In the DEM simulation, a constant shear strain rate of 0.01/s was applied in order to ensure a quasi-static condition. During the DEM simulation, the volume of RVE is kept unchanged to ensure an undrained condition. Although water is not explicitly modelled, the pore water pressure is determined by the difference between the vertical total stress and the vertical effective stress, while the latter is derived from inter-particle contact forces [4,19]. Figure 2a shows the shear stress ($\tau$) and shear strain ($\gamma$) relationship from the DEM simulation. The simulation represents a cyclic simple-shear test under a constant cyclic stress ratio (CSR) of 0.2. Figure 2b shows the evolution of shear stress ($\tau$) with the effective vertical normal stress ($\sigma_v'$). After 16 loading cycles, the soil reaches zero effective stress, i.e., the state of "initial liquefaction" [21]. The simulation result is qualitatively similar to laboratory tests of a medium dense sand. Typical cyclic behaviors can be observed from the DEM simulation, such as gradual decrease of effective vertical stress after each load cycle to the initial liquefaction, accumulation of shear strain, and phase transform from a contractive to dilative volumetric response in each loading cycle.

It is also interesting to observe different deformation patterns of the soil before and after liquefaction. Before the initial liquefaction, $\gamma_{\max}$, the maximum double-amplitude shear strain induced in each loading cycle slowly increases to about 2 % towards the initial liquefaction (cycle No. 16). Post-liquefaction deformation occurs afterwards, where $\gamma_{\max}$ increases dramatically from cycle No. 17 to 25. The increasing rate of $\gamma_{\max}$ is reduced after 25 cycles, until the maximum shear strain ceases to increase under further repeated loading. This phenomenon will be revisited and explained in the later part of this paper.

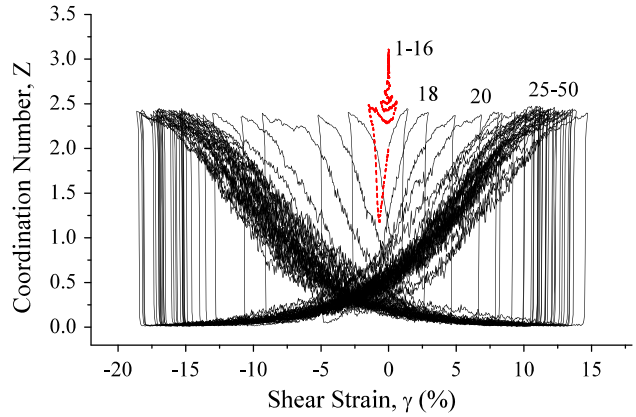


**Fig. 3** Coordination number and shear strain relation

## 3 Load-bearing structure of the granular packing in liquefaction

### 3.1 Evolution of the coordination number

The effective stress in the granular packing is transmitted through particle contacts. The condition number is a good indicator of the micromechanical load-bearing structure since it represents an average number of contacts for each particle, defined as $Z = 2N_c/N_p$ (where $N_c$ is the total number of contacts and $N_p$ is the total number of particles). Figure 3 shows the evolution of $Z$ during the cyclic loading process. The coordination number initially progressively decreases from about 3.1 to about 2.3 in the first 16 cycles, but then begins a pattern of alternating between incrementally decreasing and incrementally increasing. The cyclic variation in the contact number is qualitatively similar to the cyclic variation in the effective stress, and shows similar butterfly shaped loops in Fig. 2b after the initial liquefaction is triggered.

To have a better understanding of the post-liquefaction soil behaviors, we highlight the stress–strain relationship, stress path and evolution of the coordination number in load cycle No. 18 in Fig. 4. The complete loading cycle is labeled using 0-1-2-3-4-5-6-7 sequentially. Following unloading from point 2, the post-liquefaction shear deformation can be decomposed into a "flow stage" ($\gamma_0$), as illustrated from point 3 to point 4 in Fig. 4, and a "hardening stage" ($\gamma_d$), which is the strain from point 4 to point 5 in Fig. 4. Note that $\gamma_0$ occurs at "zero" effective confining stress state, and $\gamma_d$ occurs during non-zero effective confining stress [23]. Since a true zero effective confining stress is not achieved in both numerical simulations and experimental tests, the packing is regarded as in the 'flow stage' when effective confining stress is below 0.5 kPa (that is equivalent to a shear stress smaller than 0.2 kPa). The flow stage was followed by the hardening stage (point 1 to 2, and point 4 to 5) when the shear stress starts growing substantially to about 20 kPa.

As is shown in Fig. 4c, the number of contacts established at the end of the flow stage (i.e., point 1 and 4) is about 84 % of the number established at the peak stress point (i.e., point 2 and 5). The coordination number increases from 2 to 2.4 during the hardening stage (point 1 to 2, and point 4 to 5). These contacts form a load-bearing structure that permits stress to

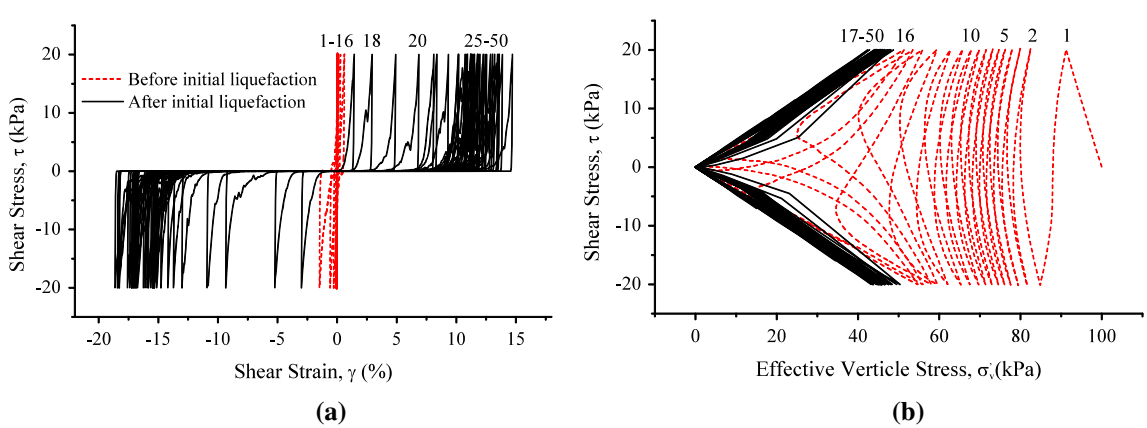


**Fig. 2** DEM simulation of a granular packing in undrained cyclic loading: **a** shear stress and shear strain relation, **b** shear stress and effective vertical stress relation

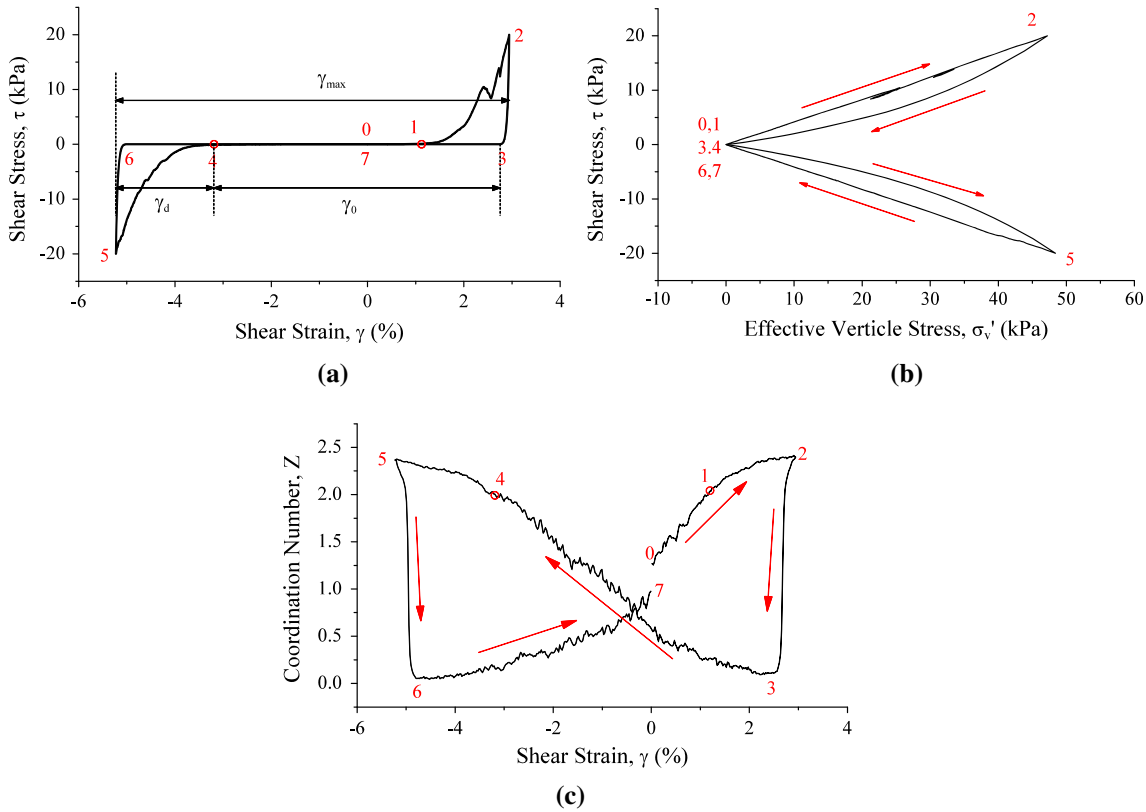


**Fig. 4** **a** Stress–strain relation, **b** stress path and **c** evolution of coordination number in post-liquefaction (loading cycle No. 18)

increase during further shear deformation. Another interesting observation from Fig. 4c is that the minimum value of the coordination number is achieved immediately upon unloading (from point 2 to 3, and from point 5 to 6), where the coordination number decreases dramatically to 0.1. It implies that the load-bearing structure is completely destroyed upon unloading. The phenomenon will be further explained using a new particle-void fabric in the later sessions.

Transition from the flow stage to the hardening stage requires a certain number of particle contacts to form a stable load-bearing structure. As is shown in Fig. 4c, the transition point (point 4) corresponds to a threshold coordination number (Z) of around 2 in the case studied. Figure 5 further illustrates the relationship between the coordination number and the shear stress in all loading cycles before and after liquefaction. When Z is below the threshold, the packing is under the flow stage and the sample can only sustain a very minimum shear stress. It is to be noted a repeated pattern of the coordination number develops immediately after the initial liquefaction, which is mainly reflective of the repeated effective stress pattern during the post-liquefaction cycles. Yet, the coordination number cannot be used to explain why the mobilized strain continues to accumulate with increasing number of loading cycles. In the later sections, we will explain that it is mainly due to continuous evolution of the internal particle-void structure in the post-liquefaction stage.

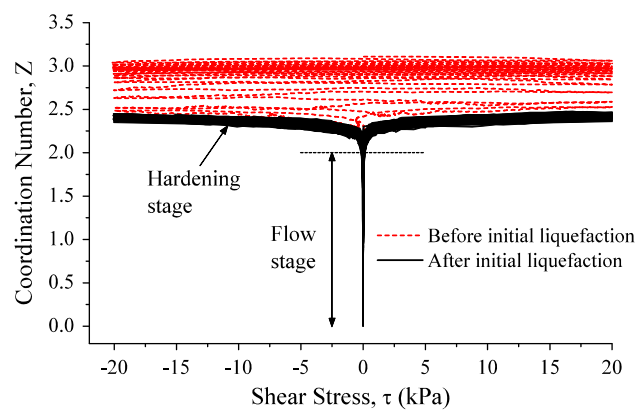


**Fig. 5** Relation between coordination number and shear stress

It should be also noted that the coordination number is a scalar quantity that can only provide an averaged measure of contacts. The inter-particle contact is actually distributed anisotropically, in response to the anisotropic stress field. For a 2D packing, rose diagram is used to visualize the angular distribution of the coordination number as shown in Fig. 6, where the radial length of the diagram represents the coordination number in a certain direction:

$$z(\theta) = \left(\frac{2\pi}{\Delta\theta}\right)\left[\frac{2N_c(\theta)}{N_p}\right] \tag{1}$$

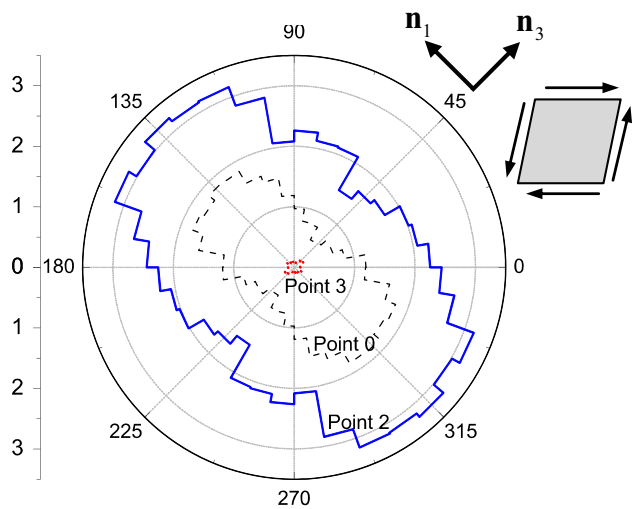


**Fig. 6** Angular distribution $z(\theta)$ of the coordination number in post-liquefaction (loading cycle No. 18)

where $N_c(\theta)$ is the number of contacts whose orientation is within an angle bin $[\theta - \Delta\theta/2, \theta + \Delta\theta/2]$, $N_p$ is the total number of particles. Note that the coordination number $Z = \frac{1}{2\pi}\int_0^{2\pi} z(\theta)d\theta$. Figure 6 compares the angular distribution $z(\theta)$ at the flow stage (point 0 in Fig. 4a), the hardening stage (point 2) and an unloading point (point 3) in cycle No. 18. The coordination numbers $z(\theta)$ have similar angular distribution at point 0 and 2. A maximum number of contacts are formed in the direction of compression ($\mathbf{n}_1$) and a minimum number of contacts in the direction of extension ($\mathbf{n}_3$). This corresponds to the formation of a strong force chain and a weak force chain in two orthogonal directions. Although a majority of compressive force is carried by the strong force chain, the weak force chain is required to prevent instability of the strong force chain. However, immediately upon unloading (from point 2 to point 3), almost all inter-particle contacts are destroyed in all directions. The granular assemblage immediately loses its loading-bearing structure and is reduced to a fully liquefied state.

### 3.2 Evolution of the non-affine displacement field

Although the coordination number is a good indicator to quantify the overall load-bearing structure of the granular packing, it cannot explain how particles are re-arranged to form such a structure. The post-liquefaction particle movement can be further demonstrated using the non-affine displacement [7].

First, the affine displacement is defined as the displacement field prescribed by a *uniform* global strain field. In this study, we use the displacement increment to highlight the change of the displacement field between each loading stage. Denoting the center position vector of a particle $i$ as $\mathbf{x}_n^{(i)}$ and $\mathbf{x}_{n+1}^{(i)}$ when the global strain is $\boldsymbol{\varepsilon}_n$ and $\boldsymbol{\varepsilon}_{n+1}$, respectively, the incremental total displacement of particle $i$ is $\Delta\mathbf{u}^{(i)} = \mathbf{x}_{n+1}^{(i)} - \mathbf{x}_n^{(i)}$. The incremental affine displacement of the particle is defined as $\Delta\mathbf{u}_0^{(i)} = \Delta\boldsymbol{\varepsilon} \cdot \mathbf{x}_n^{(i)}$, where $(\cdot)$ denotes the inner product of two vectors, $\Delta\boldsymbol{\varepsilon}$ is the global strain increment ($\Delta\boldsymbol{\varepsilon} = \boldsymbol{\varepsilon}_{n+1} - \boldsymbol{\varepsilon}_n$).

Second, the non-affine displacement is calculated by subtracting the affine displacement from the total displacement of the particle. The non-affine displacement can be regarded as the disturbance displacement over a comparison displacement that is associated with a uniform strain field at the particle location. The incremental non-affine displacement of particle $i$ is defined as:

$$\delta\mathbf{u}^{(i)} = \Delta\mathbf{u}^{(i)} - \Delta\mathbf{u}_0^{(i)} \tag{2}$$

To investigate evolution of non-affine displacement field during the post-liquefaction loading stage, shear strain in load cycle No. 18 is divided into five intervals with a strain increment $\Delta\gamma = 0.59\,\%$, as shown in Fig. 7a. The first two strain increments are the flowing stage and the last two strain increments are the hardening stage. The 3rd interval is a transitional stage when the stress just starts to grow. Figure 7b, c show the non-affine displacement field in the first and the last strain increment. Scales for the sample dimension and the magnitude of the vector field are also shown in the plots. Note that two vector fields are scaled differently in Fig. 7b, c so the pattern can be visually compared.

It can be observed that during the beginning of the flow stage, the non-affine displacement field is quite random in Fig. 7b. It is because particles are dispersed with few local contacts. Therefore, particle movement is not restricted by its surrounding particles. However, continued shear deformation will organize some particles to form bigger clusters. Relative displacement between particles in the cluster is restricted. Adjustment of relative positions mainly occurs between these clusters. Therefore, many distinctive "flow bands" and "vortices" can be observed in the hardening stage in Fig. 7c. Particles within the flow bands will normally have similar velocity with that of its surrounding particles.

We use the following correlation function to quantitatively compare two vectors associated with particle $i$ and $j$ in terms of both magnitude and direction of these vectors:

$$\rho\left(\delta\mathbf{u}^{(i)}, \delta\mathbf{u}^{(j)}\right) = \frac{2\delta\mathbf{u}^{(i)} \cdot \delta\mathbf{u}^{(j)}}{\left|\delta\mathbf{u}^{(i)}\right|^2 + \left|\delta\mathbf{u}^{(j)}\right|^2} \tag{3}$$

Note that $(\cdot)$ denotes the inner product of two vectors, and $|\ |$ denotes the magnitude of a vector. Clearly, $-1 \le \rho \le 1$. If two vectors have the same magnitude and direction, i.e., $\delta\mathbf{u}^{(i)} = \delta\mathbf{u}^{(j)}$, $\rho\left(\delta\mathbf{u}^{(i)}, \delta\mathbf{u}^{(j)}\right) = 1$. A negative correlation $\rho\left(\delta\mathbf{u}^{(i)}, \delta\mathbf{u}^{(j)}\right) = -1$ is achieved only if $\delta\mathbf{u}^{(i)} = -\delta\mathbf{u}^{(j)}$. If $\delta\mathbf{u}^{(i)}$ is normal to $\delta\mathbf{u}^{(j)}$, $\rho\left(\delta\mathbf{u}^{(i)}, \delta\mathbf{u}^{(j)}\right) = 0$.

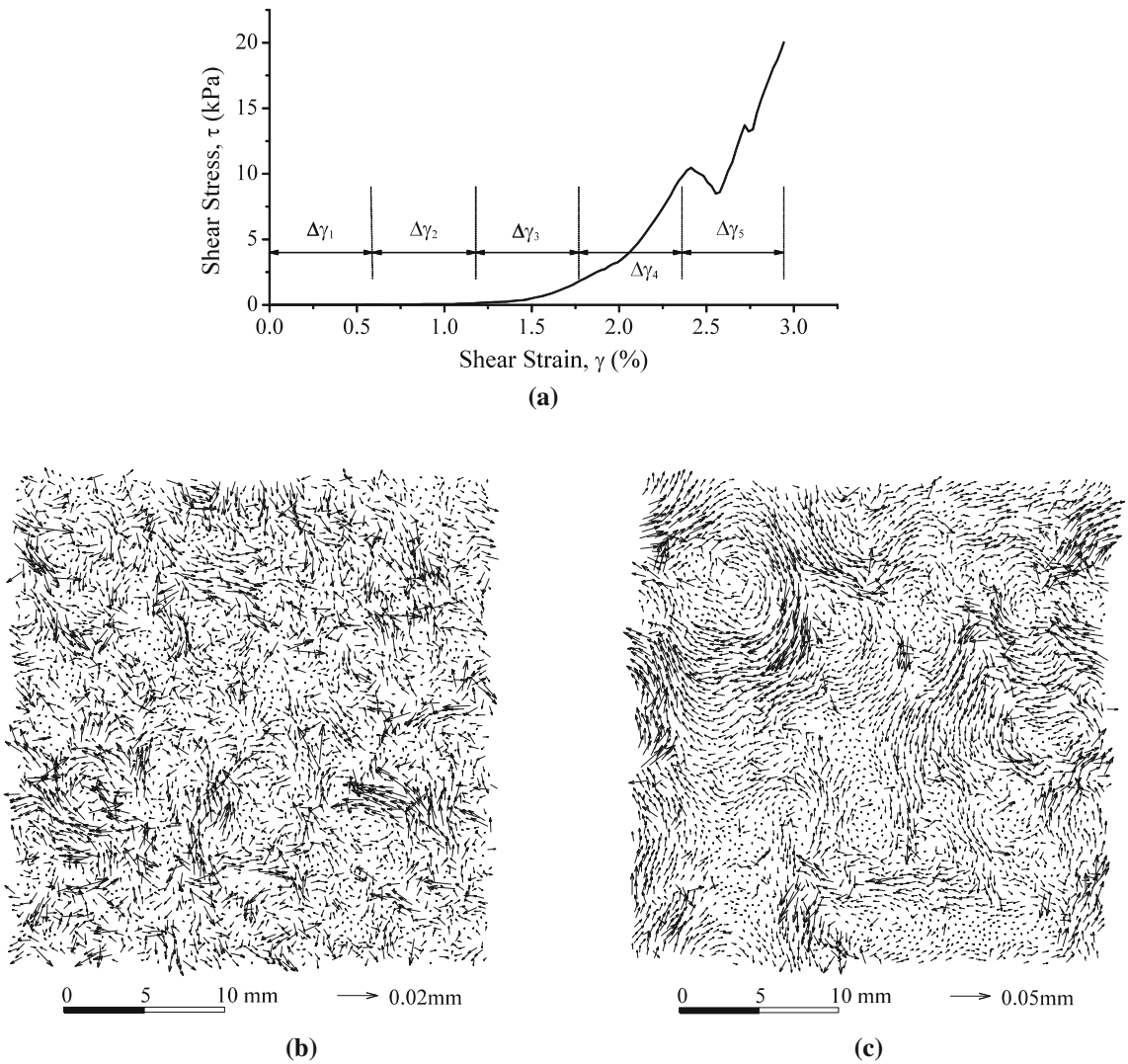


**Fig. 7** **a** Stress–strain curve and five strain increments in post-liquefaction loading cycle No. 18, **b** non-affine displacement field in 1st strain increment, and **c** in 5th strain increment

Given a separation distance $h$, a pair of particles are grouped if the center-to-center distance falls into a bin bounded by $\mathscr{B}(h) = \left[h - \frac{\Delta h}{2}, h + \frac{\Delta h}{2}\right]$, where $\Delta h$ is the size of the distance bin, set as the summation of radius of the pair of particles. The correlation function of the incremental non-affine displacement vectors associated with the particle pair, $\rho\left(\delta\mathbf{u}^{(i)}, \delta\mathbf{u}^{(j)}\right)$, is then calculated. Define $N_p(h)$ is the total number of particle pairs fall into that distance bin ($\left|\mathbf{x}^{(i)} - \mathbf{x}^{(j)}\right| \in \mathscr{B}(h)$), the spatial correlation of the incremental non-affine displacement field is defined as follows:

$$C(h) = \frac{1}{N_p(h)} \sum_{\left|\mathbf{x}^{(i)} - \mathbf{x}^{(j)}\right| \in \mathscr{B}(h)} \rho\left(\delta\mathbf{u}^{(i)}, \delta\mathbf{u}^{(j)}\right) \tag{4}$$

Figure 8 shows the spatial correlation $C(h)$ of the incremental non-affine displacement field at each loading stage, where the separation distance $h$ is normalized by mean radius $R_{50}$ (=0.3 mm) of the particle packing. It is evident that the spatial correlation decreases with increasing separation distance $h$. The correlation grows stronger from the flow stage ($\Delta\gamma_1$, $\Delta\gamma_2$) to the hardening stage ($\Delta\gamma_4$, $\Delta\gamma_5$). At the loading stage 1, C($h$) becomes negligible (<0.1) at $5R_{50}$, while at the stage 5, C($h$) $< 0.1$ only at a separation distance of $20\,R_{50}$.

## 4 Particle-void structure in liquefaction

### 4.1 The definition of $D_c$

As discussed before, the contact number reflects the load-bearing structure in response to the applied stress field. It is not sufficient to describe the internal arrangement of particles

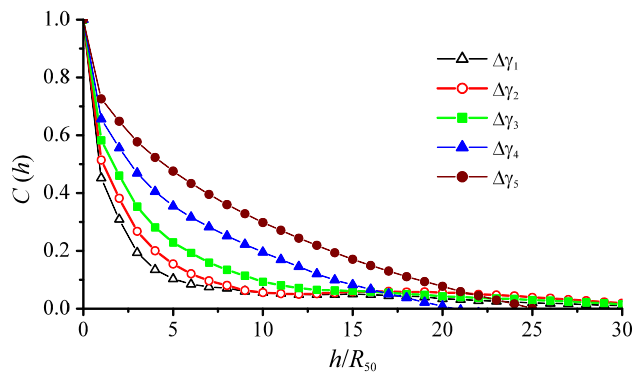


**Fig. 8** Spatial correlation of the non-affine displacement field in each strain increment

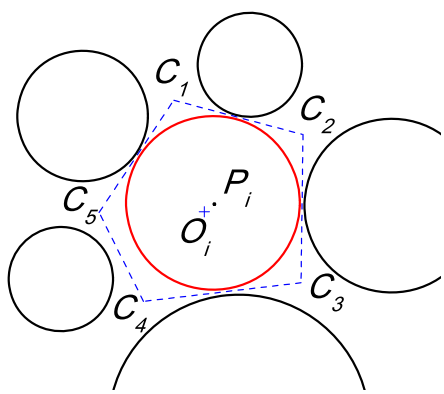


**Fig. 9** Schematic illustration of the centroid distance

and voids within the packing. For a granular soil, the Voronoi cell can be conveniently used to divide the void space around each particle. As shown in Fig. 9, the Voronoi cell for particle $i$ is a convex polygon enclosed by $C_1-C_2-C_3-C_4-C_5$. The mass center of the Voronoi cell and the mass center of the particle are denoted by vector $\boldsymbol{O}^i$ and $\boldsymbol{P}^i$, respectively. The centroid difference associated with particle $i$ is defined as a vector:

$$\boldsymbol{D}_c^{(i)} = \frac{\boldsymbol{P}^i - \boldsymbol{O}^i}{R_{50}} \tag{5}$$

whose norm is defined as:

$$D_c^{(i)} = |\boldsymbol{D}_c^{(i)}| \tag{6}$$

where $R_{50}$ is the mean particle radius of the granular packing. For each particle in the granular packing, its mobility is restricted by its surrounding particle. Centroid difference defined here is used to quantify the geometrical arrangement between the particle and its surrounding void.

The centroid distance ($D_c$) of the entire packing can be defined as the average of $D_c^{(i)}$ over all particles:

$$D_c = \frac{1}{N_p}\sum_{i=1}^{N_p} D_c^{(i)} \tag{7}$$

where $N_p$ is the total number of particles.

### 4.2 $D_c$ as a fabric index of particle-void distribution

To illustrate the evolution of particle-void distribution, snapshots at the start of cyclic loading (under a confining pressure of 100 kPa) and after 50 loading cycles (under zero confining pressure) are demonstrated in Fig. 10. They correspond to the same portion of the granular packing. Before cyclic loading, the centroid distance of the packing $D_c$ is 0.047. Particles with $D_c^{(i)} > 2D_c$ are filled in grey color for easy identification. Relatively large pores can be found surrounding these filled particles in Fig. 10a. Therefore, $D_c^{(i)}$ reflects the distribution of the void space surrounding the particles. Particles surrounded by relatively large pores usually have a larger value of $D_c^{(i)}$.

The presence of relatively large pores can be regarded as source of inhomogeneity in the granular packing. Due to friction between granular particles or complex particle shape, local arching can be formed during the initial consolidation, which preserves the large pores. However, the arching structure is not cyclically stable and can be destroyed by the cyclic loading. After 50 loading cycles, large pores diminish as shown in Fig. 10b. $D_c$ of the packing also decreases to 0.038. It is interesting to mention that Youd [35] once suggested that the pore water pressure buildup of sands during cyclic loading is due to the collapse of the looser and more unstable arrays of particles within the sand. Our observation of the particle-void redistribution corroborates Youd's suggestion.

The probability density function of $D_c$ for the granular packing before and after cyclic loading is illustrated in Fig. 11. The figure clearly shows that the proportion of large $D_c$ decreases during cyclic loading. Therefore, the net effect of undrained cyclic loading is to redistribute these relatively large pores, and cause $D_c$ to decrease as a general trend. On the other hand, large pores could be occupied by particles and granular packing would be densified under drained cyclic loading. In all these processes, large pores are redistributed and the packing structure is more homogeneous in terms of the particle-void distribution. This process is believed to be irreversible.

### 4.3 Evolution of $D_c$ and cyclic mobility

Figure 12 shows the evolution of $D_c$ during 50 loading cycles. Before the initial liquefaction, the change of $D_c$ is very small. Most rapid decrease in $D_c$ is experienced from cycle No. 16-25. Afterwards, $D_c$ repeatedly increases and decreases within

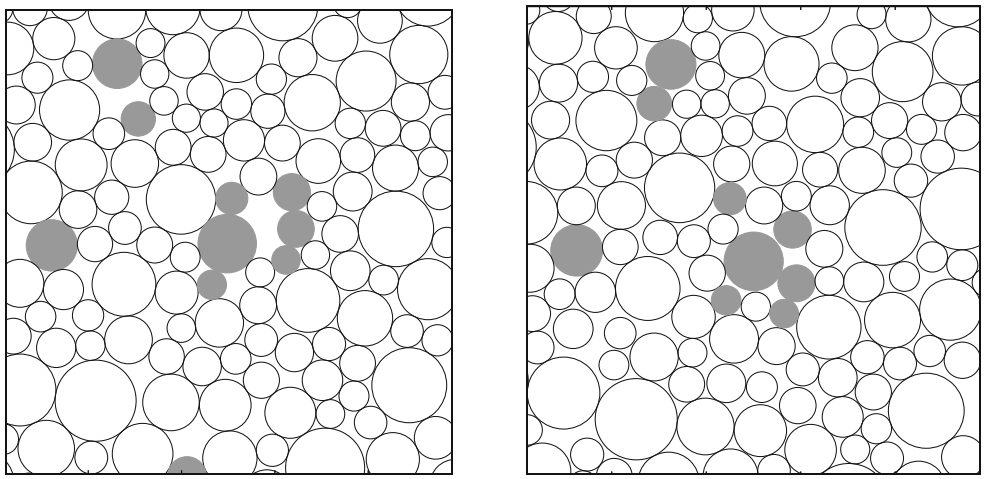


**Fig. 10** Particle-void distribution (only a 5 × 5 mm portion of the whole packing is shown), **a** before cyclic loading, $D_c = 0.047$; **b** after 50 loading cycles, $D_c = 0.038$

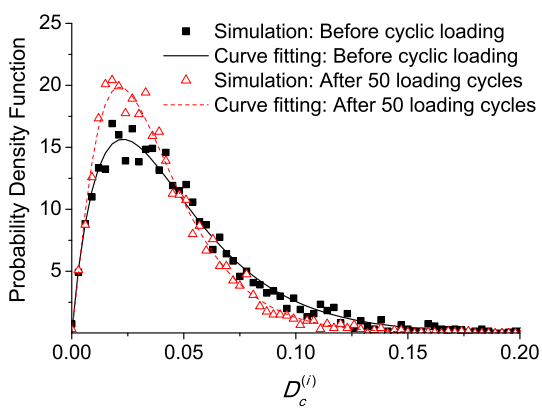


**Fig. 11** Probability density function of $D_c$ before and after cyclic loading

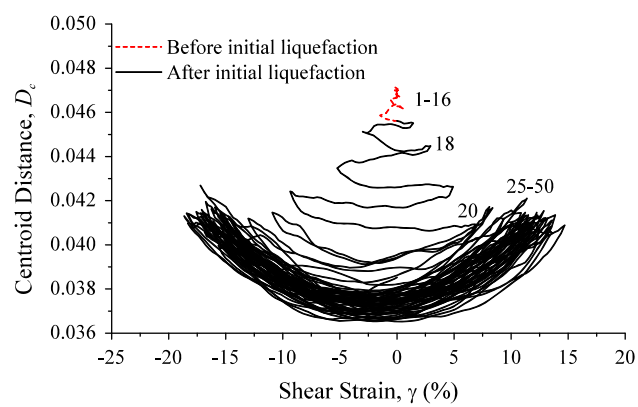


**Fig. 12** Evolution $D_c$ during 50 loading cycles

a loading cycle, with a net effect that $D_c$ decreases at the end of the cycle. However, the decreasing rate gradually slows down. The evolution pattern of $D_c$ is almost identical after 30 loading cycles.

Change in $D_c$ can be regarded as a reflection of the packing structure adjustment (redistribution of relatively large pores). Based on the evolution of $D_c$, it is possible to visualize the microscopic behavior of the granular packing during the stress-controlled cyclic loading. Within the first several cycles, the soil has not reached the liquefaction stage. Very little change in the particle-void structure can be observed in the packing. However, even such a little change will cause the mean effective stress to decrease cycle by cycle until the initial liquefaction occurs. Adjustment of the microstructure mainly happens within the post-liquefaction stage, especially during the first several cycles after the initial liquefaction.

In a stress-controlled cyclic simple-shear test, the maximum double-amplitude shear strain ($\gamma_{\max}$) developed in the soil continues to accumulate with increasing number of loading cycles, which is regarded as the cyclic mobility (cf. Fig. 2). Through the DEM simulation, we observed that the cyclic mobility of the granular packing is strongly correlated to the evolution of $D_c$. The relation between $\gamma_{\max}$ and $D_c$ is demonstrated in Fig. 13, where $D_{c,min}$ refers to the minimum $D_c$ value attained within a loading cycle. Interestingly, significant change in $D_{c,min}$ and $\gamma_{\max}$ occurs from cycle No. 16 (the initial liquefaction) to No. 25. When $D_{c,min}$ reaches to its lower-bound limit, $\gamma_{\max}$ also stabilizes around a constant value. The stress–strain curve of the soil is also stabilized. The above observation proves that the post-liquefaction deformation is closely related to the evolution of the particle-void fabric.

### 4.4 Evolution of $D_c$ with different CSRs and void ratios

Using the same packing as illustrated in Fig. 1 under the same initial state (void ratio of 0.228, initial confining pressure $p =$

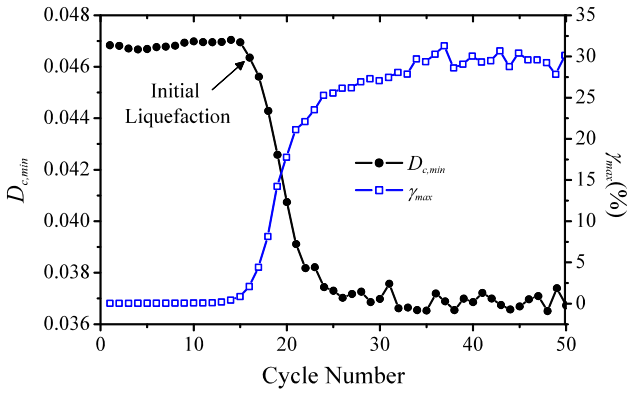


**Fig. 13** Relation between $D_{c,min}$ and $\gamma_{max}$

100 kPa), three different cyclic stress ratios (CSR = 0.17, 0.20 and 0.25) are applied to the packing. The evolution of $D_{c,min}$ are demonstrated in Fig. 14a. Several features can be readily observed from the simulations: (1) If a smaller CSR is applied, more loading cycles are needed for the packing to reach the initial liquefaction; (2) After initial liquefaction, it takes about eight to ten loading cycles to reduce $D_{c,min}$ to the lower-bound limit in all simulations. The lower-bound limit is not much affected by the CSRs.

The decreasing trend of $D_{c,min}$ can also be observed from all other DEM simulations we have conducted on samples of different densities and different particle shapes. Figure 14b demonstrates the influence of packing density. All three samples are subjected to an initial confining pressure $p = 100$ kPa and CSR = 0.25. A denser sample (i.e., a smaller void ratio) has a smaller initial $D_{c,min}$ value, and $D_{c,min}$ will reach a smaller lower-bound limit. From Fig. 14b, we can also observe that a packing with higher density needs more cycles to liquefy, which is consistent with laboratory tests (e.g., [29]). It is also worth pointing out that although it is not reported in details in this paper, a similar decreasing trend of $D_{c,min}$ can also be observed using elongated particles, implying that the trend is not affected by the particle shape.

Since $D_c$ is defined to quantify the particle-void fabric, decrease in $D_{c,min}$ implies redistribution and reduction of relatively large pores to smaller pores during cyclic loading. After each loading cycle, the packing is getting more homogeneous in terms of particle-void distribution. The existence of the lower-bound limit of $D_c$ implies that a stable state for the particle-void arrangement can be achieved eventually, if continued cyclic deformation is applied on the sample. The stable state of particle-void fabric is related to sample density, but seems to be not affected by the loading magnitude and stress path applied.

## 5 Anisotropic angular distribution of $D_c$

After initial liquefaction, the soil experiences flow deformation and then followed by strain hardening upon loading, when the sample can sustain considerable shear load. However, after unloading, the soil immediately liquefies. Figure 15a illustrates the stress–strain relationship in the loading cycle No. 46. Figure 15b shows considerable variation of $D_c$ during the loading, unloading and reloading process. In these figures, point A denotes a fully liquefied state. Point B and point C represent a hardening state during loading and reloading.

Since $D_c$ is a scalar quantity averaged over the whole sample, it does not carry information regarding the spatial distribution of the particle-void structure. In the following, we define two variables to quantify the angular distribution of vector $\boldsymbol{D}_c$ in terms of an averaged value and the relative density. First, we define:

$$\bar{D}_c(\theta) = \frac{1}{N(\theta)} \sum_{dir(\boldsymbol{D}_c^{(i)}) \in \mathscr{B}(\theta)} D_c^{(i)} \tag{8}$$

where $N(\theta)$ is the number of $\boldsymbol{D}_c$ whose vector direction falls into an angular bin defined by $\mathscr{B}(\theta) = [\theta - \Delta\theta/2, \theta + \Delta\theta/2]$, i.e., $dir\left(\boldsymbol{D}_c^{(i)}\right) \in \mathscr{B}(\theta)$. Note that Eq. (8) represents an aver-

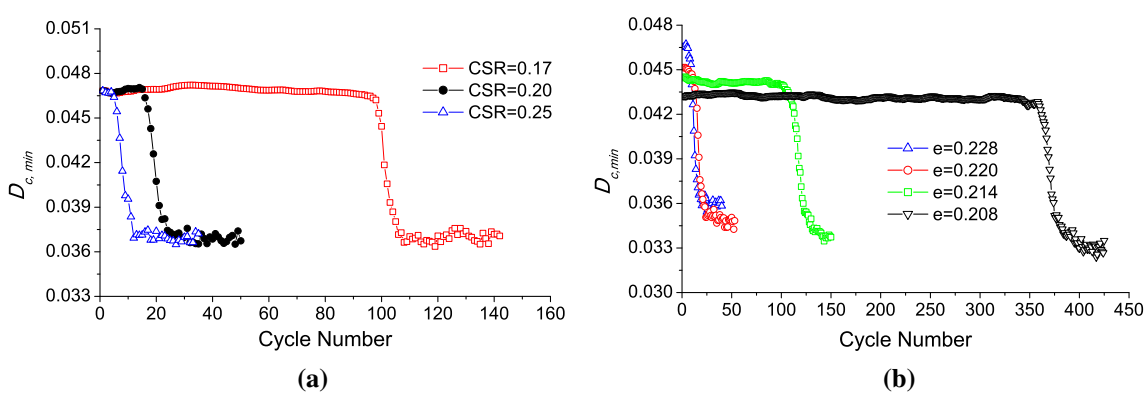


**Fig. 14** **a** Evolution of $D_c$ with different CSRs; **b** evolution of $D_c$ with different void ratios

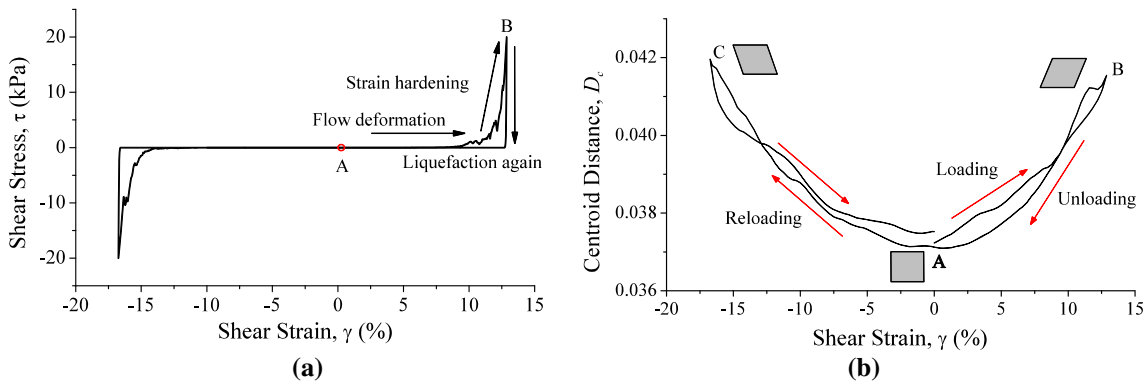


**Fig. 15** **a** Stress–strain relationship, and **b** evolution of $D_c$ in post-liquefaction (loading cycle No. 46)

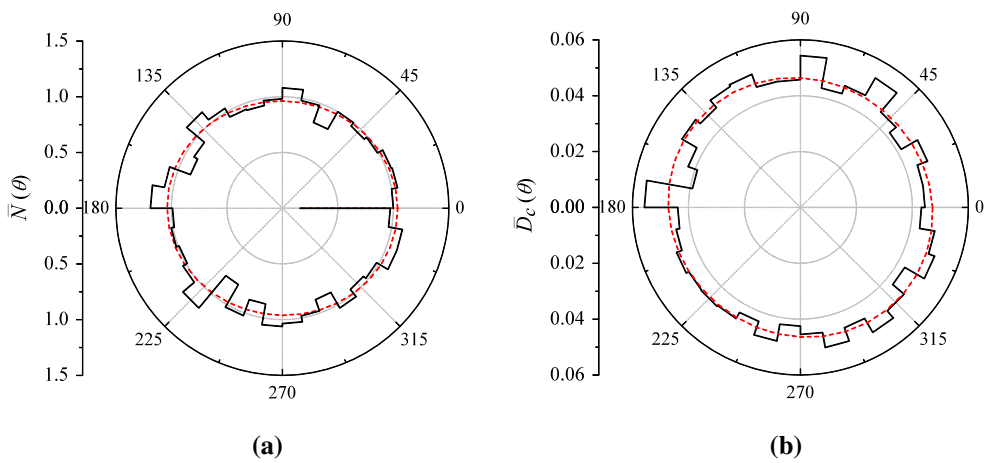


**Fig. 16** The angular distribution $\bar{N}(\theta)$ and $\bar{D}_c(\theta)$ at the initial state of packing. Degrees of anisotropy for $\bar{N}(\theta)$ and $\bar{D}_c(\theta)$ are 0.039 and 0.027 respectively

aged centroid distance in an angular direction. Further, we define:

$$\bar{N}(\theta) = \frac{2\pi N(\theta)}{N_p \Delta\theta} \tag{9}$$

where $N_p$ is the total number of particles in the packing. Therefore, $\bar{N}(\theta)$ defines the relative number (density) of $\boldsymbol{D}_c$ whose vector direction falls into bin $\mathscr{B}(\theta)$. It is obvious that if the relative density of $\boldsymbol{D}_c$ vector is isotropically distributed, $\bar{N}(\theta) = 1$.

The polar histograms in Figs. 16 and 17 (solid lines) demonstrate the angular distribution of $\bar{N}(\theta)$ and $\bar{D}_c(\theta)$ obtained from the sample at different loading stages. Note the vertical axis shows the scale used to measure the magnitude of $\bar{N}(\theta)$ or $\bar{D}_c(\theta)$ in different orientations. The sample distribution can be approximated by a simple, smooth function (dashed lines in Figs. 16, 17) using the following procedure.

For the two-dimensional case, the sampled distribution can be expanded by the Fourier series. Let $X(\theta)$ represents either $\bar{N}(\theta)$ or $\bar{D}_c(\theta)$, it can be written as:

$$\begin{aligned} X(\theta) &= \frac{1}{2\pi}\int_0^{2\pi} X(\theta)d\theta + \sum_{n=1}^{+\infty} c_n \cos n\,(\theta - \theta_n) \\ &= a_0 + \sum_{n=1}^{+\infty} c_n \cos n\,(\theta - \theta_n) \end{aligned} \tag{10}$$

where $a_0 = \frac{1}{2\pi}\int_0^{2\pi} X(\theta)d\theta$. If the periodicity of the distribution $X(\theta) = X(\theta + \pi)$ is assumed, and higher order terms are neglected (cf. Rothenburg and Bathurst [19]), the above expansion can be approximated using only two Fourier terms as:

$$X(\theta) = a_0\,[1 + a_c \cos 2\,(\theta - \theta_c)] \tag{11}$$

where $a_c = \frac{c_2}{a_0}$, $\theta_c = \theta_2$ can be readily obtained from Eq. (10). Note that $a_c$ is a parameter defining the degree of anisotropy of the angular distribution. $a_c = 0$ represents the isotropic distribution, i.e, a circle in the polar histogram. $\theta_c$ defines the major principal direction of the anisotropy.

The polar histogram in Fig. 16 demonstrates the angular distribution of $\bar{N}(\theta)$ and $\bar{D}_c(\theta)$ at the initial state of the

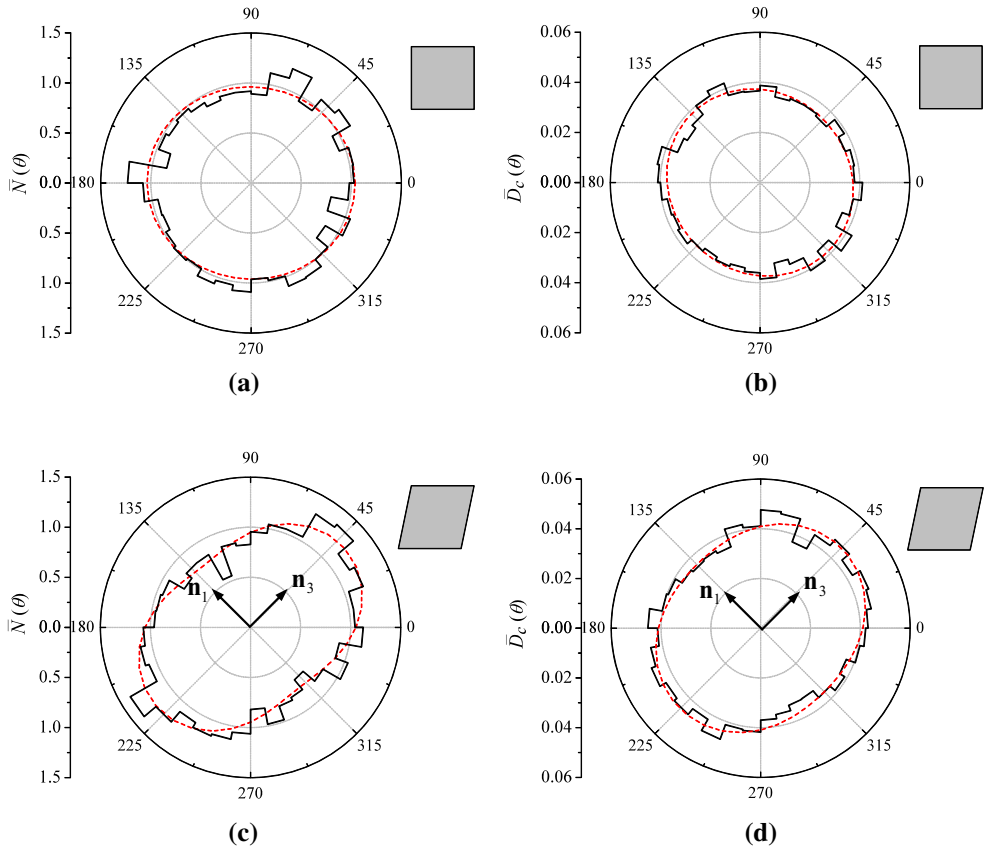


**Fig. 17** The angular distribution $\bar{N}(\theta)$ and $\bar{D}_c(\theta)$ at different states in cycle No. 46: **a**, **b** a fully liquefied state at point A in Fig. 15. Degrees of anisotropy for $\bar{N}(\theta)$ and $\bar{D}_c(\theta)$ are 0.041 and 0.040 respectively. **c**, **d**: a hardening state at point B in Fig. 15. Degrees of anisotropy for $\bar{N}(\theta)$ and $\bar{D}_c(\theta)$ are 0.227 and 0.117 respectively

packing (unliquefied). The dashed line in Fig. 16 is the fitted curve using the Fourier form in Eq. (11). The magnitude of anisotropy is so small that the angular distribution is nearly isotropic.

During the post-liquefaction stage, the angular distribution of $\bar{N}(\theta)$ and $\bar{D}_c(\theta)$ varies within a loading cycle. Referring to Fig. 15, $D_c$ peaks up from a liquefied state A ($\gamma = 0\,\%$) to a hardening state B ($\gamma = 12.8\,\%$). The angular distribution of $\bar{N}(\theta)$ and $\bar{D}_c(\theta)$ at these states is demonstrated in Fig. 17. At the fully liquefied state A in Fig. 17a, the angular distribution of $\bar{N}(\theta)$ and $\bar{D}_c(\theta)$is almost isotropic, which is similar to the unliquefied initial state (Fig. 16) except that the magnitude of $\bar{D}_c(\theta)$ is smaller. At the hardening state B in Fig. 17b, the angular distribution of $\bar{N}(\theta)$ and $\bar{D}_c(\theta)$is highly anisotropic with the major principal direction of anisotropy in the direction of $\mathbf{n}_3$. Degrees of anisotropy for $\bar{N}(\theta)$ and $\bar{D}_c(\theta)$ are 0.227 and 0.117 respectively.

Figure 18 visualizes the particle-void distribution and force chain of the packing at point B. Most strong force chains are located along compression direction $\mathbf{n}_1$ with relatively large pores on either side. In the previous discussion, we

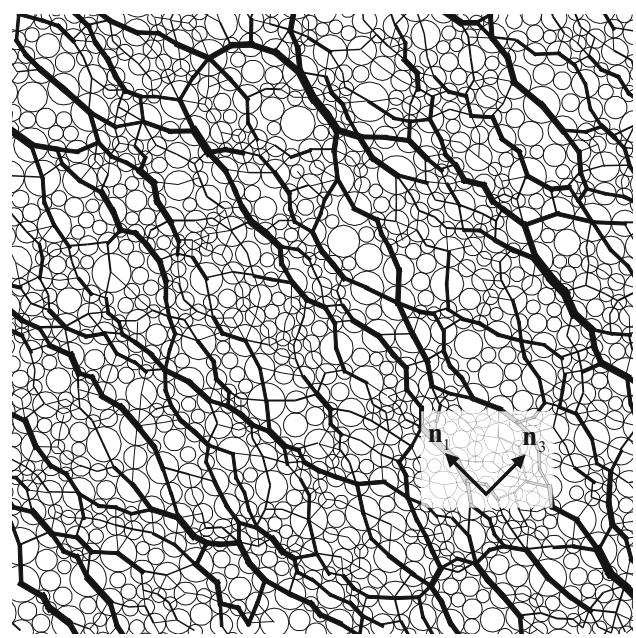


**Fig. 18** Particle configuration and force chain of the packing at state B (only a 15 × 15 mm portion of the whole packing is shown)

have mentioned that the initial relatively large pores would be redistributed by cyclic loading. Similarly, shear deformation could also reorganize relatively large pores when the packing is loaded from A to B. The reorganized large pores are not distributed randomly. Rather, relative to a solid particle, large pores have higher possibility to be located along $\mathbf{n}_3$ due to extension in that direction. As a result, $d_c(\theta)$ is highly anisotropic, with the maximum value attained in the extension direction ($\mathbf{n}_3$), and minimum value in the compression direction ($\mathbf{n}_1$), as shown in Fig. 17b. The anisotropic particle-void fabric implies a highly anisotropic load-bearing capability. Immediately upon unloading, the internal particle-void fabric has not been changed. Large voids in $\mathbf{n}_3$ direction have to be compressed first before a strong force chain can be formed in that direction. Indeed, the packing will immediately collapse to a fully liquefied state and experience flow deformation. Only through the flow deformation can these relatively large pores be redistributed again, until a new particle-void fabric is formed together with strong force chains developed in $\mathbf{n}_3$ direction in the reloading process.

## 6 Conclusions

In this paper, the micromechanical behavior of granular materials in cyclic mobility and post-liquefaction stage is investigated using DEM. The post-liquefaction stress–strain behavior is characterized by a flow stage followed by a strain hardening stage. In the flow stage, although the effective stress is almost zero, a load-bearing structure is gradually formed. During the formation of such a load-bearing structure, relative position adjustment of particles will be concentrated between bigger clusters, as evidenced by the non-affine displacement field. The distribution of coordination number can be used to represent the load-bearing structure, which is highly anisotropy and is closely related to the stress field. However, under repeated cyclic loading, the coordination number ceases to evolve immediately after the initial liquefaction. The loading-bearing structure in the form of particle contact can be easily destroyed in the post-liquefaction stage immediately upon unloading.

To represent the particles and voids distribution in the assemblage, the difference between the particle center and the Voronoi cell center is defined as "centroid distance" ($D_c$), which is independent of the particle contact. Physically, $D_c$ reflects the spatial distribution of voids around the particles. Particles with relatively large pores around have higher probability to have large value of $D_c$. The index is found to be effective to characterize the change in the internal structure of the granular packing even after liquefaction. Using $D_c$ as an indicator, the following microstructure evolution is observed during undrained cyclic loading:

(a) The number of particles with a large value of $D_c$ dereases during undrained cyclic loading, reflecting redistribution of relatively large pores before and after liquefaction. The process is believed to be irreversible.
(b) It is observed that cyclic mobility and post-liquefaction deformation of the granular packing is strongly correlated to the evolution of $D_c$. The $D_c$ of the packing decreases with increasing number of cycles until it reaches a lower-bound limit. Meanwhile, the mobilized maximum shear strain also stops increasing and is stabilized around a constant value.
(c) The lower-bound limit of $D_c$ implies a stable state of particle-void distribution can be achieved in post-liquefaction. The limit is influenced by packing density, but seems not be affected by cyclic stress ratio and loading path that the soil takes to reach the limit.
(d) Highly anisotropic angular distribution of $D_c$ is observed during the post-liquefaction stage, implying a highly anisotropic particle-void structure, and correspondingly, highly anisotropic loading-bearing capability.

The micromechanical study provides significant insight to understand the cyclic mobility and post-liquefaction process. Although two-dimensional DEM simulations are conducted in this study, similar behaviors would be expected in 3D simulations, which will be conducted in the future.

**Acknowledgments** The study was financially supported by General Research Fund Grant No. 16213615, Research Project Competition (UGC/HKUST) Grant No. RPC11EG27 and Theme-based Research Scheme Grant No. T22-603/15N from Hong Kong Research Grants Council.

## References

1. Ashmawy, A.K., Sukumaran, B., Hoang, V.V.: Evaluating the influence of particle shape on liquefaction behavior using discrete element modeling. Proc. 13th Int. Offshore Polar Eng. Conf. ISOPE Honol. **2**, 542–549 (2003)
2. Bray, J., Sancio, R.: Assessment of the liquefaction susceptibility of fine-grained soils. J. Geotech. Geoenviron. Eng. **132**(9), 1165–1177 (2006)
3. Castro, G.: Liquefaction and cyclic mobility of saturated sands. J. Geotech. Eng. Div. ASCE **101**(GT6), 551–569 (1975)
4. Christoffersen, J., Mehrabadi, M.M., Nemat-Nasser, S.: A micromechanical description of granular material behavior. J. Appl. Mech. **48**, 339–44 (1981)
5. Dafalias, Y.F., Manzari, M.T.: Simple plasticity sand model accounting for fabric change effect. J. Eng. Mech. ASCE **130**(6), 622–634 (2004)
6. Elgamal, A., Yang, Z., Parra, E., Ragheb, A.: Modeling of cyclic mobility in saturated cohesionless soils. Int. J. Plast. **19**(6), 883–905 (2003)
7. Goldenberg, C., Tanguy, A., Barrat, J.L.: Particle displacements in the elastic deformation of amorphous materials: local fluctuations vs. non-affine field. Europhys. Lett. **80**, 16003 (2007)

8. Gu, X., Huang, M., Qian, J.: DEM investigation on the evolution of microstructure in granular soils under shearing. Granul. Matter **16**, 91–106 (2014)
9. Guo, N., Zhao, J.: The signature of shear-induced anisotropy in granular media. Comput. Geotech. **47**, 1–15 (2013)
10. Idriss, I.M., Boulanger, R.W.: Semi-empirical procedures for evaluating liquefaction potential during earthquakes. Soil Dyn. Earthq. Eng. **26**, 115–130 (2006)
11. Idriss, I.M., Boulanger, R.W.: Soil Liquefaction During Earthquakes. Earthquake Engineering Research Institute, Oakland, California (2008)
12. Ishihara, K.: Liquefaction and flow failure during earthquakes. Géotechnique **43**(3), 351–415 (1993)
13. Kramer, S.L.: Geotechnical Earthquake Engineering, 1st edn. Prentice Hall, New Jersey (1996)
14. Li, X., Li, X.S.: Micro-macro quantification of the internal structure of granular materials. J. Eng. Mech. ASCE **135**(7), 641–656 (2009)
15. Mitchell, J., Soga, K.: Fundamentals of Soil Behavior. Wiley, New York (2005)
16. Ng, T.T., Dobry, R.: Numerical simulations of monotonic and cyclic loading of granular soil. J. Geotech. Eng. ASCE **120**(2), 388–403 (1994)
17. O'Sullivan, C.: Particulate Discrete Element Modelling, A Geomechanics Perspective. Spon Press, Oxon, UK (2011)
18. Radjaï, F., Wolf, D.E., Jean, M., Moreau, J.J.: Bimodal character of stress transmission in granular packings. Phys. Rev. Lett. **80**, 61–64 (1998)
19. Rothenburg, L., Bathurst, R.J.: Analytical study of induced anisotropy in idealized granular materials. Géotechnique **39**(4), 601–614 (1989)
20. Satake, M.: Fabric tensor in granular materials. In: Proceedings IUTAM Conference on Deformation and Failure of Granular Materials, Delft, pp. 63–67 (1982)
21. Seed, H.B., Lee, K.L.: Liquefaction of saturated sands during cyclic loading. J. Soil Mech. Found. Div. ASCE **92**(SM6), 105–134 (1966)
22. Seed, R.B., Cetin, K.O., Moss, R.E.S., et al.: Recent advances in soil liquefaction engineering: a unified and consistent framework. EERC Report 2003-06, University of California, Berkeley (2003)
23. Shamoto, Y., Zhang, J.M., Goto, S.: Mechanism of large post-liquefaction deformation in saturated sand. Soils Found. **37**(2), 71–80 (1997)
24. Shire, T., O'Sullivan, C., Barreto, D., Gaudray, G.: Quantifying stress-induced anisotropy using inter-void constrictions. Géotechnique **63**(1), 85–91 (2013)
25. Sitar N.: Slope stability in coarse sediments. In: Yong, R.N. (ed.) Special Publication on Geological Environmental and Soil Properties, ASCE, pp. 82–98 (1983)
26. Sitharam, T.G., Vinod, J.S., Ravishankar, B.V.: Post-liquefaction undrained monotonic behavior of sands: experiments and DEM simulations. Géotechnique **59**(9), 739–749 (2009)
27. Šmilauer, V., Catalano, E., Chareyre, B., Dorofeenko, S., Duriez, J, Gladky, A., Kozicki, J., Modenese, C., Scholtès, L., Sibille, L., Stránský, J., Thoeni, K.: Yade documentation. In: Šmilauer V., (ed.) The Yade Project, 1st edn. http://yade-dem.org/doc/ (2010)
28. Thornton, C.: Numerical simulations of deviatoric shear deformation of granular media. Géotechnique **50**(1), 43–53 (2000)
29. Vaid, Y.P., Sivathayalan, S.: Static and cyclic liquefaction potential of Fraser Delta sand in simple shear and triaxial tests. Can. Geotech. J. **33**(2), 281–289 (1996)
30. Vaid, Y.P., Stedman, J.D., Sivathayalan, S.: Confining stress and static shear effects in cyclic liquefaction. Can. Geotech. J. **38**(3), 580–591 (2001)
31. Wang, G., Xie, Y.: Modified bounding surface hypoplasticity model for sands under cyclic loading. J. Eng. Mech. ASCE **140**(1), 91–104 (2014)
32. Wang, Z.L., Dafalias, Y.F., Shen, C.K.: Bounding surface hypoplasticity model for sand. J. Eng. Mech. ASCE **116**(5), 983–1001 (1990)
33. Yang, J., Sze, H.Y.: Cyclic behaviour and resistance of saturated sand under non-symmetrical loading conditions. Géotechnique **61**(1), 59–73 (2011)
34. Ye, J.H., Wang, G.: Seismic dynamics of offshore breakwater on liquefiable seabed foundation. Soil Dyn. Earthq. Eng. **76**, 86–99 (2015)
35. Youd, T.L.: Packing changes and liquefaction susceptibility. J. Geotech. Eng. Div. ASCE **103**(8), 918–922 (1977)
36. Youd, T.L., Idriss, I.M., Andrus, R.D., Ignacio, A., Gonzalo, C., Christian, J.T., Dobry, R., Finn, W.D.L., et al.: Liquefaction resistance of soils: summary report from the 1996 NCEER and 1998 NCEER/NSF workshops on evaluation of liquefaction resistance of soils. J. Geotech. Geoenviron. Eng. ASCE **127**(10), 297–313 (2001)
37. Zhao, J., Guo, N.: Unique critical state characteristics in granular media considering fabric anisotropy. Géotechnique **63**, 695–704 (2013)
38. Zienkiewicz, O.C., Chan, A.H.C., Pastor, M., Schrefler, B.A., Shiomi, T.: Computational Geomechanics: With Special Reference to Earthquake Engineering. Wiley, New York (1999)